International Journal of Multiphase Flow 68 (2015) 80–92

Contents lists available at ScienceDirect

International Journal of Multiphase Flow

journal homepage: www.elsevier.com/locate/ijmulflow

Modelling of gas–solid turbulent channel flow with non-spherical particles with large Stokes numbers

Berend van Wachem *, Marian Zastawny, Fan Zhao, George Mallouppas

Division of Thermofluids, Department of Mechanical Engineering, Imperial College London, Exhibition Road, London SW7 2AZ, United Kingdom

ARTICLE INFO

Article history:
Received 7 March 2013
Received in revised form 3 October 2014
Accepted 9 October 2014
Available online 22 October 2014

Keywords:
Non-spherical particles
Turbulent gas–solid flow
Large eddy simulation

ABSTRACT

This paper describes a complete framework to predict the behaviour of interacting non-spherical particles with large Stokes numbers in a turbulent flow. A summary of the rigid body dynamics of particles and particle collisions is presented in the framework of Quaternions. A particle-rough wall interaction model to describe the collisions between non-spherical particles and a rough wall is put forward as well. The framework is coupled with a DNS-LES approach to simulate the behaviour of horizontal turbulent channel flow with 5 differently shaped particles: a sphere, two types of ellipsoids, a disc, and a fibre. The drag and lift forces and the torque on the particles are computed from correlations which are derived using true DNS.

The simulation results show that non-spherical particles tend to locally maximise the drag force, by aligning their longest axis perpendicular to the local flow direction. This phenomenon is further explained by performing resolved direct numerical simulations of an ellipsoid in a flow. These simulations show that the high pressure region on the acute sides of a non-spherical particle result in a torque if an axis of the non-spherical particle is not aligned with the flow. This torque is only zero if the axis of the particle is perpendicular to the local direction of the flow. Moreover, the particle is most stable when the longest axis is aligned perpendicular to the flow.

The alignment of the longest axis of a non-spherical particle perpendicular to the local flow leads to non-spherical particles having a larger average velocity compared to spherical particles with the same equivalent diameter. It is also shown that disc-shaped particles flow in a more steady trajectory compared to elongated particles, such as elongated ellipsoids and fibres. This is related to the magnitude of the pressure gradient on the acute side of the non-spherical particles. Finally, it is shown that the effect of wall roughness affects non-spherical particles differently than spherical particles. Particularly, a collision of a non-spherical particle with a rough wall induces a significant amount of rotational energy, whereas a corresponding collision with a spherical particle results in mostly a change in translational motion.

Introduction

Knowledge of the dynamics of turbulent gas–solid flows has a great importance for the successful design and determination of optimum operating conditions of numerous industrial applications, e.g. pneumatic transport, cyclone separators, fluidised beds, dust collectors, and pulverised-coal combustors to name a few. These systems exhibit complex flow dynamics and interactions between flow components. In particular, the complexity of the interaction between particles and gas-phase turbulence (Vreman, 2007) and the effect of particle–particle and particle–wall collisions (Sommerfeld and Kussin, 2003) have stimulated research work in recent years.

Turbulent gas–solid flows have been studied experimentally (e.g. Snyder and Lumley, 1971; Kulick et al., 1994; Kussin and Sommerfeld, 2002) and numerically. Numerical simulations can be done in an ensemble-averaged framework, in which the particle properties are represented by their mean or a PDF (e.g. Simonin et al., 1993; Minier and Peirano, 2001; van Wachem et al., 2001a). Alternatively, the location and other properties of each individual particle can be tracked, the so-called Lagrangian approach (e.g. Tsuji, 1993; Tsuji et al., 1992; van Wachem et al., 2001b; Kuang et al., 2008). With this approach, various frameworks can be used to account for the interaction of the particle with the surrounding fluid. Most common is the so-called "point-particle" approach, in which an empirical expression is used to estimate the interaction

* Corresponding author. Tel.: +44 20 759 47030; fax: +44 20 759 45702.
E-mail address: Berend.van.Wachem@gmail.com (B. van Wachem).

http://dx.doi.org/10.1016/j.ijmultiphaseflow.2014.10.006
0301-9322/

between the fluid and the particle, which is added as a momentum source to the fluid. A valid empirical relation between the local fluid properties and the interaction forces for the specific particle must exist in order to use this approach. Moreover, a point-source approach is only valid if the particle is sufficiently small with respect to the Kolmogorov scale of the fluid. Otherwise, a more detailed coupling algorithm must be used, which takes into account the no-slip condition on the surface of each particle (e.g. Patankar et al., 2000; Mittal and Iaccarino, 2005; Mark and van Wachem, 2008). Although this type of coupling is more accurate, it is also computationally very expensive and currently very restrictive in the number of particles it can deal with.

The majority of studies involving gas-particle flows assume that particles are perfect spheres. This assumption is very convenient because of several factors: perfect spheres are simple to model, their behaviour is well known, and lastly there is a large availability of models in the literature which describe the particle–fluid interactions (e.g. Fan and Zhu, 1998). However, assuming the particles are perfect spheres may be unrealistic, because most applications deal with non-spherical particles. Analysis of flows with non-spherical particles is considerably more complicated than flows with spherical particles. While a sphere is characterised by its diameter only, even a very simple non-spherical particle like a disc or a fibre needs at least two parameters to be uniquely defined. This makes the rigid body dynamics of non-spherical particles more complex than the corresponding dynamics of spherical particles. Moreover, additional complexities arise in describing the interaction of a non-spherical particle with a fluid. In a uniform flow a sphere experiences only a drag force, whereas a non-spherical body is also affected by a transverse lift force, a pitching torque and a counter-rotational torque. Moreover, all of these forces acting on a non-spherical body depend not only on the Reynolds number, but also on the angle between the axes of the particle and the direction of the incoming flow. Additionally, the framework for describing collisions requires a different approach compared to the one used for perfect spheres; for instance, the orientation of the particle must be taken into account. All of the factors above contribute to the complexity of the investigated problem and are addressed throughout this article.

A comprehensive overview of the available methods to describe the shape, the resulting drag force based on correlations and their associated behaviour of non-spherical particles is presented in Chhabra et al. (1999), Mandø and Rosendahl (2010). A common approach to describe the particle shape is by using a so-called "sphericity factor", Φ (Wadell, 1934). Sphericity is defined as the ratio of the surface area of a sphere over the surface area of a non-spherical particle with the equivalent volume. By definition, the sphericity is less than or equal to one. In most engineering handbooks (e.g. Crowe, 2005) and papers (e.g. Hölzer and Sommerfeld, 2008) the drag of a non-spherical particle is estimated from correlations for spherical particles which are modified to take into account the sphericity factor.

The majority of papers concerning the simulation of the behaviour of non-spherical particles use the framework of Brenner (1964) to determine the hydrodynamic drag interaction and Jeffery (1922) to describe the hydrodynamic torque acting on a particle from a flow (e.g. Marchioli et al., 2010; Marchioli and Soldati, 2013; Njobuenwu and Fairweather, 2013; Zhao and van Wachem, 2013a). However, both models assume creeping flow and Stokes flow conditions, and are in principle not valid to describe gas-particle flows where there is a slip between the particle and fluid velocity. Hence, simulations carried out using these models cannot resolve gas-particle flows with non-spherical particles, where there is a slip between the particle and the fluid flow, *i.e.* particles with finite Stokes numbers.

In Zastawny et al. (2012), the development of models for the drag, lift and torques acting on non-spherical particles with a significant slip has been researched by means of true direct numerical simulation. The term "true" emphasises that not only all the flow scales are resolved but also a no-slip boundary condition is applied at the surface of particle. As all the existing flow scales are resolved, there are no assumptions required at this scale to capture the interaction of the particles with the fluid flow. The true direct numerical simulations in this paper are shown to be grid independent, and a large number of simulations have been performed for each particle shape. Although there is a good agreement from the new drag, lift and torque model with the analytical models of Brenner (1964) and Jeffery (1922), the models show that the behaviour of non-spherical particles at larger slip velocities is quite different from the models put forward by Brenner (1964) and Jeffery (1922).

The most notable difference of the forces on a non-spherical particle in a flow with a significant slip velocity, is the detachment of the flow at the acute edges on the particles. This is illustrated by a result of the resolved direct numerical simulation shown in Fig. 1. This figure shows an ellipsoid in a flow with a slip velocity between the particle and the fluid, the Reynolds number based on the slip velocity is 200. It can be clearly seen that the acute edges of the particle cause the flow to separate. This leads to high pressure regions near these points of detachment, as is indicated by the colours of Fig. 1. This was also confirmed in Hölzer and Sommerfeld (2008).

These high pressure regions cause a net fluid torque to act on the particle, and as a consequence the particle will rotate until the pressure gradients are of equal magnitude on both sides of the particle. Thus, the configuration as shown in Fig. 1 is unstable, and the resulting net torque on the particle originates from the difference in pressure gradients on either side of the particle. This will result in a rotation of the particle in the flow, until the pressure gradients are maximum and of equal magnitude on both sides of the particle. Hence, a non-spherical particle will tend to maximise its drag once there is a slip velocity between the particle and the fluid. This is also commonly observed in nature, as described for instance in Hoerner (1965): leaves that fall from a tree do not fall as fast as possible, but maximise their drag and their falling time. There are numerous other examples of this in nature.

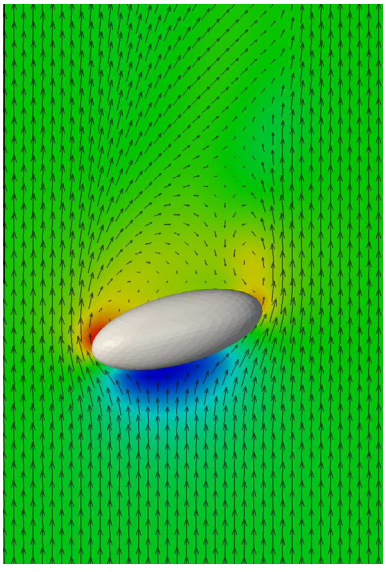

Fig. 1. A snapshot of an ellipsoid in a flow with significant slip ($Re_p = 200$). The vectors indicate the flow velocity and the colours indicate the relative pressure.

In studying the orientation of non-spherical particles with a slip velocity between the particle and the fluid, the application of the drag and torque model as put forward by Brenner (1964) and Jeffery (1922) is not applicable. The application of these models will not result in the particles to have a preferred orientation with respect to the mean flow, as has been shown in numerous papers (Marchioli et al., 2010; Zhao and van Wachem, 2013a). However, as discussed above, for the gas-particle case with a slip velocity between the fluid and the particle, a preferred orientation is to be expected.

The aim of this paper is to investigate the influence of the particle shape on interacting particles flowing in a horizontal turbulent channel flow, for particles with a significant Stokes number. To achieve this, large eddy simulations (LES) of a horizontal turbulent channel flow laden with five different particle shapes, incorporating the drag, lift and toque model derived in Zastawny et al. (2012), are performed. The well-documented horizontal channel flow case described in Kussin and Sommerfeld (2002), who study spherical particles, is used as a reference case. The measurements in their work was done with phase Doppler anemometry (PDA), to measure the fluid and particle velocity simultaneously. The numerical framework applied in this paper has been previously validated for *spherical* particles in Mallouppas and van Wachem (2013). In that paper, it is shown that the comprehensive discrete element model (DEM) is more accurate in determining the behaviour of the particles in this horizontal gas–solid channel flow that the hard-sphere model. Moreover, this paper showed that the fluid mechanics are accurately modelled using the LES framework. In the current paper, this framework is extended to account for non-spherical particles.

The details of the five particles researched in this article are shown in Table 1. The results of the simulations are compared to experimental and numerical data for spheres and the effect of non-sphericity will be discussed. Moreover, the effect of wall roughness of the channel walls on the behaviour of the five different particle shapes is researched and is shown to be very important.

In the large-scale simulation of non-spherical particles the true DNS framework, where the flow around each particle is calculated, is not yet feasible because of the large number of particles and the relatively high *Re* number. Therefore, a point-source approximation of particles in the flow combined with LES is pursued (e.g. Portela and Oliemans, 2003). This approach relaxes the necessity to resolve the flow around each individual particle. The individual particles are not "seen" by the fluid, but their presence is approximated through momentum source terms and, if applicable, a local volume fraction. The momentum source terms arise from approximations of the drag and lift forces. The simulations are four-way coupled, that is the effect of the fluid on the particles, the effect of the particles on the fluid, and the effect of particle–particle and particle–wall collisions are all taken into account. The individual components of the models are described in the following sections.

Table 1
The size, shape and sphericity of the five particles considered in this paper. Also, the definition of the angle of attack is shown.

Shape	Sphericity	Proportions	Size
Sphere 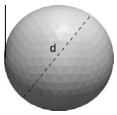	1		200 μm
Ellipsoid 1 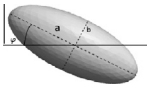	0.885	$\frac{a}{b}=\frac{5}{2}$	$a=368$ μm $b=147$ μm
Ellipsoid 2 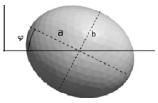	0.991	$\frac{a}{b}=\frac{5}{4}$	$a=232$ μm $b=186$ μm
Disc 	0.626	$\frac{a}{b}=5$	$a=342$ μm $b=68.4$ μm
Fibre 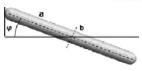	0.639	$\frac{a}{b}=5$	$a=510$ μm $b=102$ μm

Fluid phase modelling

The Reynolds number of the flow experimentally examined by Kussin and Sommerfeld (2002) is far too high to make DNS a feasible option. In Sommerfeld (2003) an empirical velocity profile and velocity fluctuations are assumed. It is also possible to use the Reynolds averaged Navier–Stokes (RANS) approach to determine the flow, although this requires a significant amount of empirical parameters and a non-trivial treatment of the boundary layer near the wall.

In this research paper, large eddy simulation (LES) is pursued. In this approach, there are no fitting parameters (Sagaut, 2005) and the resulting filtered momentum equations are

$$\frac{\partial(\rho^f\widetilde{v}_j^f)}{\partial t}+\frac{\partial(\rho^f\widetilde{v}_j^f\widetilde{v}_i^f)}{\partial x_i}=-\frac{\partial\widetilde{p}}{\partial x_j}+\frac{\partial(\widetilde{\tau}_{ij})}{\partial x_i}-\frac{\partial(\tau_{ij}^a)}{\partial x_i}+S_j^f+\beta_{(f,p)}\left(\widehat{\widetilde{v}}_j^f-\widetilde{v}_j^p\right) \quad (1)$$

where $\widetilde{v}^f$ represents the filtered fluid velocity and $\widetilde{v}^p$ the particle velocity in the *Eulerian* framework. The last two terms on the right hand side of Eq. (1) represent the general source terms, S_j^f and the momentum exchange between the fluid phase and the particle phase. The fluid velocity in the inter-phase momentum exchange term is the undisturbed fluid velocity, therefore it is denoted by $\widehat{\widetilde{v}}^f$.

The equations arising from filtering are very similar to the Navier–Stokes equations, except for the addition of one term, describing the behaviour of the sub-grid scale (SGS) stresses, namely τ_{ij}^a. To close the subgrid-scale stresses, two different approaches have been applied: the Smagorisnky model with van-Driest damping near the wall and the dynamic model proposed by Germano et al. (1991) and Lilly (1992). Both models are outlined further and the results are compared to each other for horizontal turbulent channel flow in Mallouppas and van Wachem (2013). In Mallouppas and van Wachem (2013) it is shown that the framework gives an accurate prediction of the flow dynamics; various LES models are compared with each other and with the experimental data.

Dynamics of non-spherical particles

Although the motion or dynamics of a spherical particle is relatively straightforward (e.g. van Wachem et al., 2001b), the dynamics of a non-spherical particle are more complicated. The rigid body dynamics of a non-spherical particle concern its motion and behaviour during one or more collisions. The ordinary differential equation describing the translational position and velocity are the same as for a spherical particle (Newton's second law),

$$\frac{D\boldsymbol{v}_p}{Dt}=\boldsymbol{a}_p \quad (2)$$

$$\rho_p V_p\boldsymbol{a}_p=\underbrace{\boldsymbol{F}_D}_{\text{drag}}+\underbrace{\boldsymbol{F}_L}_{\text{lift}}+\underbrace{V_p\rho_p\boldsymbol{g}}_{\text{gravity}}+\underbrace{V_p\nabla P}_{\text{Archimedes}}+\underbrace{\rho_p V_p\boldsymbol{a}_c}_{\text{collisions}} \quad (3)$$

where V_p is the volume of the particle, ρ_p the density, $\boldsymbol{v}_p$ the velocity of the particle in the *Lagrangian* framework, and $\boldsymbol{a}_c$ represents

the forces due to collisions, which will be discussed later. The added mass and history forces are neglected in the equation, as they are not significant in the case studied in this paper. All the forces are combined in the acceleration term $\boldsymbol{a}_p$. The position and velocity are solved using the Verlet scheme (Allen and Tildesley, 1989),

$$\boldsymbol{x}_p(t+\Delta t) = 2\boldsymbol{x}_p(t) - \boldsymbol{x}_p(t-\Delta t) + \boldsymbol{a}_p(t)\Delta t^2 + O(\Delta t^4) \tag{4}$$

$$\boldsymbol{v}_p(t+\Delta t) = \frac{\boldsymbol{x}_p(t+\Delta t) - \boldsymbol{x}_p(t-\Delta t)}{2\Delta t} + O(\Delta t^2) \tag{5}$$

The velocity is determined with less accuracy than the position, but this is not essential in this scheme, as the velocity itself is not directly involved in updating the position of the particle; *i.e.* Eq. (4) does not directly depend on the velocity.

The rotational motion of a non-spherical particle is very different compared to that of a spherical particle. For a non-spherical particle the orientation is important, unlike for a spherical particle. To derive the rotational equations of motion for a non-spherical particle, it is convenient to introduce two types of Cartesian spaces: body space and world space, see Fig. 2. For all variables in body space, the superscript b is employed. All variables without this superscript represent the variables in world space.

Rotation by Quaternions

Due to the absence of singularity and Gimbal lock problems (e.g. Evans and Murad, 1977), unit Quaternions are increasingly popular to represent rotation of a non-spherical particle. General Quaternions do not only change the orientation of a vector, but also scale the length of a vector. Therefore, the equation for representing rotation cannot be a simple Quaternion multiplication, as the length of the vector could change. To represent rotation by Quaternions, the length of the Quaternions must be exactly unity. Rotation without scaling is performed by unit Quaternions, see Eberly (2002), Hoffmann (1978).

Quaternions were first introduced by Sir Hamilton (Hamilton, 1844; Gsponer and Hurni, 1993) in the nineteenth century and are widely used to represent rotation for modelling dynamic systems in the past decades. They are expressed in a complex number system, consisting of a scalar part and a vector part. Hence, there are a total of 4 unknowns. In dynamics, the physical meaning of a Quaternion is to scale the length and change the orientation of a vector (Ibanez, 2001). A Quaternion is defined by:

$$q = [q_0, \boldsymbol{q}] \tag{6}$$

where q_0 is the scalar part, and $\boldsymbol{q}$ is the vector part. A vector $\boldsymbol{s}$ rotated by a pair of unit Quaternions is defined by

$$\boldsymbol{s}' = q\boldsymbol{s}q^{-1} \tag{7}$$

where q is a unit Quaternion, q^{-1} represents the conjugation of q,

$$q^{-1} = [q_0, -\boldsymbol{q}] \tag{8}$$

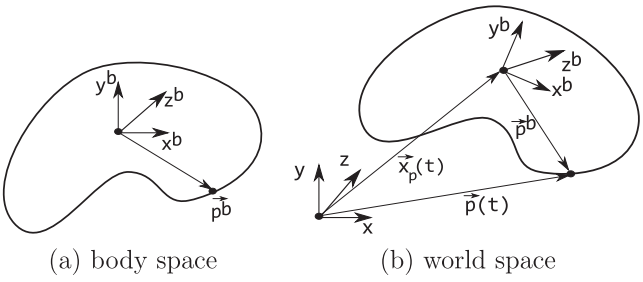

Fig. 2. The relation between body space (a) and world space (b). The fixed axes of body space, x^b, y^b and z^b are indicated in both figures. The position of a fixed point in body space, p^b is transformed to world space, $p(t)$.

and the vector $\boldsymbol{s}$ is interpreted as a Quaternion as $s = [0, \boldsymbol{s}]$, thus with the scalar part of the Quaternion equal to zero. The multiplication of two Quaternions is defined by the Grassman product,

$$pq = [p_0 q_0 - \boldsymbol{pq}, p_0\boldsymbol{q} + q_0\boldsymbol{p} + \boldsymbol{p}\times\boldsymbol{q}] \tag{9}$$

The unit Quaternion q can be directly expressed in a form containing the vector around which the rotation takes place and the angle of the rotation (Betsch and Siebert, 2009; Karney, 2007)

$$q = \left[\cos\frac{\alpha}{2}, \sin\frac{\alpha}{2}\hat{\boldsymbol{q}}\right] \tag{10}$$

where $\hat{\boldsymbol{q}}$ is the normalised vector around which the rotation takes place and the angle α indicates the rotational angle. In the unit Quaternion q, the coefficients q_0, q_1, q_2 and q_3 are sometimes referred to as Euler parameters (e.g. Betsch and Siebert, 2009), which are not independent of each other, as they must always satisfy

$$\|q\| = \sqrt{q_0^2 + q_1^2 + q_2^2 + q_3^2} = 1 \tag{11}$$

Many integration algorithms do not inherently respect this constraint and explicitly re-normalise the Quaternion after the algorithm is applied, by defining the corrected Quaternion as

$$\hat{q} = \frac{q}{\sqrt{q_0^2 + q_1^2 + q_2^2 + q_3^2}} \tag{12}$$

This is, however, not the same as inherently embedding the unit length of the Quaternion, as expressed by Eq. (11), into the algorithm itself. Applying Eq. (12) affects the relation between the four parameters of the Quaternion, therefore modifying the rotation it represents.

Most research papers applying Quaternions to represent the orientation of non-spherical particles still determine the corresponding rotation matrix explicitly to perform the rotation of vectors and tensors. Obtaining the rotation matrix requires an inverse relationship between rotation matrices and unit Quaternions and may introduce additional inaccuracies. Therefore, the current article uses Quaternions only, without the necessity of computing the rotation matrix. The rotation of a vector by a Quaternion is given by Eq. (7). The transformation of second order tensors by unit Quaternions can be expressed as

$$\bar{\bar{I}}' = \left(q\left(q\bar{\bar{I}}q^{-1}\right)^T q^{-1}\right)^T \tag{13}$$

Following the above analysis, unit Quaternions can be used to transform vector properties during rotation, but also to transform tensors properties directly. Accordingly, rotation matrices can be completely replaced by corresponding unit Quaternions only, and the rotation matrix is no longer required. This will save a significant amount of computer memory (4 instead of 9 floating point numbers per particle), and increase the accuracy introduced by round-off errors, as fewer operations are required.

Rigid body dynamics

The equations of motion describing non-spherical rigid particles consist of translational and rotational components. The position of a particle can be described equally simple in world space and in body space, but for the orientation of a particle the equations are significantly more complex in world space than body space. To describe the rotation of non-spherical particles, the most common and convenient way is to compute rotational properties of particles in body space and, if required, transform them into world space. The governing dynamic equations are determined by the angular momentum equations in body space, and the differential equation of the angular momentum is given by

$$\dot{\boldsymbol{L}}^b + \boldsymbol{\omega}^b \times \boldsymbol{L}^b = \boldsymbol{\tau}^b \tag{14}$$

where the $\boldsymbol{L}^b$ represents angular momentum, the $\boldsymbol{\omega}^b$ is angular velocity and $\boldsymbol{\tau}^b$ is torque acting on the body. The superscript b means the variables are evaluated in the body space framework. The angular momentum is related to the angular velocity by

$$\boldsymbol{L}^b = \bar{\bar{I}}^b \boldsymbol{\omega}^b \tag{15}$$

where the second order tensor $\bar{\bar{I}}^b$ is the moment of inertia in body space, which is constant for a rigid body. The time derivative of angular momentum in Eq. (14) is determined by

$$\dot{\boldsymbol{L}}^{\boldsymbol{b}} = \dot{\bar{\bar{I}}}^b \boldsymbol{\omega}^b + \bar{\bar{I}}^b \dot{\boldsymbol{\omega}}^b \tag{16}$$

in which the first item on the right hand side of the above equation is equal to zero, because the tensor $\bar{\bar{I}}^b$ is constant. Therefore, the angular acceleration is given as

$$\dot{\boldsymbol{\omega}}^b = \overline{\overline{I^b}}^{-1} (\boldsymbol{\tau}^b - \boldsymbol{\omega}^b \times \overline{\overline{I^b}} \boldsymbol{\omega}^b) \tag{17}$$

Numerical integration of Quaternions

The method to numerically integrate the unit Quaternion put forward in this paper approximates the angular velocity with a basic Lie–Euler method. In this paper, we propose the application of the predictor–corrector direct multiplication (PCDM) method (Zhao and van Wachem, 2013b), which is not based on Taylor series, but applies the predictor–corrector and direct multiplication algorithms.

Firstly, the variables which describe the rotational motion of a particle are transformed into body space from world space at current time level n

$$\boldsymbol{\omega}_n^b = q_n^{-1} \boldsymbol{\omega}_n q_n \tag{18}$$

$$\boldsymbol{\tau}_n^b = q_n^{-1} \boldsymbol{\tau}_n q_n \tag{19}$$

The angular velocity expressed in body space at the mid-point of the next time level, $\boldsymbol{\omega}^b_{n+\frac{1}{2}}$ and at a quarter of next time level, $\boldsymbol{\omega}^b_{n+\frac{1}{4}}$, are determined by

$$\begin{aligned} \boldsymbol{\omega}^b_{n+\frac{1}{4}} &= \boldsymbol{\omega}^b_n + \frac{1}{4} \dot{\boldsymbol{\omega}}^b_n \delta t \\ \boldsymbol{\omega}^b_{n+\frac{1}{2}} &= \boldsymbol{\omega}^b_n + \frac{1}{2} \dot{\boldsymbol{\omega}}^b_n \delta t \end{aligned} \tag{20}$$

where the angular acceleration in body space, $\dot{\boldsymbol{\omega}}^b$, is given by Eq. (17). The predicted angular velocity at a quarter at next time level in world space, $\boldsymbol{\omega}_{n+\frac{1}{4}}$, can be directly based on the unit Quaternion q_n

$$\boldsymbol{\omega}_{n+\frac{1}{4}} = q_n \boldsymbol{\omega}^b_{n+\frac{1}{4}} q_n^{-1} \tag{21}$$

Then, a *prediction* of the unit Quaternion at the half time interval, $q'_{n+\frac{1}{2}}$, is determined by the velocity $\boldsymbol{\omega}_{n+\frac{1}{4}}$. The prime on the variable emphasises that it concerns a *prediction* of the variable, not its final value.

$$q'_{n+\frac{1}{2}} = \left[\cos \frac{\|\boldsymbol{\omega}_{n+\frac{1}{4}}\| \delta t}{4}, \sin \frac{\|\boldsymbol{\omega}_{n+\frac{1}{4}}\| \delta t}{4} \frac{\boldsymbol{\omega}_{n+\frac{1}{4}}}{\|\boldsymbol{\omega}_{n+\frac{1}{4}}\|} \right] q_n \tag{22}$$

Using this predicted unit Quaternion $q'_{n+\frac{1}{2}}$, the angular velocity $\boldsymbol{\omega}_{n+\frac{1}{2}}$ at mid-point of next time level in world space is determined by

$$\boldsymbol{\omega}_{n+\frac{1}{2}} = q'_{n+\frac{1}{2}} \boldsymbol{\omega}^b_{n+\frac{1}{2}} q'^{-1}_{n+\frac{1}{2}} \tag{23}$$

Then, the corrected unit Quaternion q_{n+1} at the new time level can be determined as

$$q_{n+1} = \left[\cos \frac{\|\boldsymbol{\omega}_{n+\frac{1}{2}}\| \delta t}{2}, \sin \frac{\|\boldsymbol{\omega}_{n+\frac{1}{2}}\| \delta t}{2} \frac{\boldsymbol{\omega}_{n+\frac{1}{2}}}{\|\boldsymbol{\omega}_{n+\frac{1}{2}}\|} \right] q_n \tag{24}$$

Finally, the angular velocity in body space at the new time level can be determined and transformed to the angular velocity in world space,

$$\boldsymbol{\omega}^b_{n+1} = \boldsymbol{\omega}^b_n + \dot{\boldsymbol{\omega}}^b{}_{n+\frac{1}{2}} \delta t \tag{25}$$

$$\boldsymbol{\omega}_{n+1} = q_{n+1} \boldsymbol{\omega}^b_{n+1} q^{-1}_{n+1} \tag{26}$$

The method as outlined above presents a consistent and accurate predictor–corrector direct multiplication (PCDM) method to determine the unit Quaternion representing the orientation of a non-spherical particle and its angular velocity. Moreover, this method does not use a rotation matrix and does not mix time-levels inconsistently in its final correction (Zhao and van Wachem, 2013b). In Zhao and van Wachem (2013b) the PCDM method is compared to other numerical integration schemes for non-spherical particles, and is validated using 3 test cases. This paper showed that the PCDM method has an increased order of accuracy compared to other methods, and conserves both momentum and energy. Moreover, the method is validated with a number of analytical solutions.

Determining the mass middle point and moment of inertia

The non-spherical particles are assumed rigid and homogeneous, which implies that the density, ρ_p, throughout the particles is constant. The mass of a particle is then given by

$$m_p = \rho_p V_p \tag{27}$$

There is no simple equation for calculating the mass and mass centre of a non-spherical particle directly. However, it is straightforward to do this by first determining the volume of the particle computationally. The volume is determined by generating points in an imaginary box enclosing the particle. The ratio of points which fall inside the particle, N_p, over the total number of points, N, gives the ratio of the volume of the particle over the volume of the imaginary box, as the total number of tried points becomes very large,

$$\frac{V_{body}}{V_{box}} = \lim_{N \to \infty} \frac{N_p}{N} \tag{28}$$

The centre of mass of the non-spherical particle can be found in a similar way, by summing over the positions of the imaginary points which fall inside the particle, $\boldsymbol{r}_p$,

$$\boldsymbol{x}_p(t) = \lim_{N_p \to \infty} \frac{1}{N_P} \sum_{n=1}^{N_p} \boldsymbol{r}_{p,n}(t) \tag{29}$$

In order to determine the moment of inertia, a similar method as outlined above is employed, where a different expression is used for the diagonal terms as for the non-diagonal terms,

$$I^b_{p,ii} = \frac{m_p}{N_P} \lim_{N_p \to \infty} \sum_{n=1}^{N_p} (\boldsymbol{r}^{\boldsymbol{b}}_{p,n,j} - \boldsymbol{x}^{\boldsymbol{b}}_{p,j})^2 + \left(\boldsymbol{r}^{\boldsymbol{b}}_{p,n,k} - \boldsymbol{x}^{\boldsymbol{b}}_{p,k} \right)^2 \tag{30}$$

(*summation over j and k*)

$$I^b_{p,ij} = I^b_{p,ji} = \frac{m_p}{N_P} \sum_{n=1}^{N_p} (\boldsymbol{r}^{\boldsymbol{b}}_{p,n,i} - \boldsymbol{x}^{\boldsymbol{b}}_{p,i}) \cdot (\boldsymbol{r}^{\boldsymbol{b}}_{p,n,j} - \boldsymbol{x}^{\boldsymbol{b}}_{p,j}) \;\; \forall i \neq j \tag{31}$$

The moment of inertia in body space is constant, and is expressed as $\bar{\bar{I}}^b$, and the relation between the moment of inertia in body space and world space is determined by application of Eq. (13). The moment of inertia in world space thus depends on the orientation of the non-spherical particle and varies with time. It needs to be recomputed at every time step by application of Eq. (13).

Contact detection

At sufficient high particle loadings both particle–particle and particle–wall collisions are important for predicting the behaviour

of the flow. Therefore, all potential collisions must be correctly detected in order to determine their contribution. Moreover, the particle–wall collisions are required to keep the particles in the domain. There are various frameworks to describe particle collisions. In the hard-sphere, or event driven, framework the collisions are dealt with using global conservation of momentum and energy. In the soft-sphere framework, the dynamics of the actual collision are resolved, using approximations from elasticity theory.

In this paper we consider the soft-sphere approach, thus contact forces and torques are determined for particles which are actually slightly overlapping. This overlap is a representation for the local deformation, or displacement, and a Hertzian force model can be used to predict the resulting repellent force. Therefore, each pair of near-neighbour particles is checked for overlap. This is possible through describing the particle surfaces with a mathematical function (Delaney and Cleary, 2010) or by building the body from spheres (Langston et al., 2004). In this work, we have pursued the latter approach. Each body is then filled with a number of overlapping fictitious spheres, typically with varying radii, where the number of fictitious spheres determines the accuracy of the surface representation of the body. An example is shown in Fig. 3. This framework allows for a similar contact detection approach as for spherical particles, as described, for instance, in Allen and Tildesley (1989).

Rough wall modelling

The effect of rough walls has shown to be important in a number of gas-particle flows because the particles that collide with a rough wall have a tendency to be re-suspended into the flow more often (Sommerfeld and Kussin, 2004). In particle-laden horizontal channel flow simulations, neglecting the effect of wall roughness predicts a large number of particles "grazing" the bottom wall. It is shown experimentally by Kussin and Sommerfeld (2002) that the wall roughness strongly enhances the transverse dispersion of the particles and their fluctuating velocities throughout the channel. The measurements have also revealed that the wall roughness causes a significant reduction of the mean horizontal velocity of the particles. Numerical simulations of this flow have also been able to show these effects (Mallouppas and van Wachem, 2013; Konan et al., 2011; Lain and Sommerfeld, 2007).

The most obvious approach to model a rough wall is a deterministic approach, where the wall roughness is resolved. However, because of the rapidly changing normal of the wall, a fully deterministic approach is quite costly. Therefore, a stochastic approach to model wall roughness is adopted. There are a number of stochastic approaches described in the literature (e.g. Tsuji et al., 1987; Fukagata et al., 2001), the most frequently applied model is of Sommerfeld (1992), later corrected for the so-called shadow effect, in Sommerfeld and Huber (1999). A stochastic model usually works with a virtual wall concept, which changes the orientation of the wall with angle γ, which is sampled from an experimentally determined distribution of wall roughness.

Using the soft-sphere model, as done in this work, the collision between a particle and the wall is fully resolved. To account for this deterministic nature of the collision, a novel wall roughness model was derived and validated in Mallouppas and van Wachem (2013). The results of this novel rough wall model for soft-sphere collisions provides very good results, the same as the rough wall model for hard-sphere collisions as put forward in Sommerfeld and Huber (1999) and the further improvements to account for secondary collision effects by Konan et al. (2009). These secondary collision effects are inherently captured by the wall roughness model for soft-sphere collisions. The algorithm for the rough wall can be summarised for collision with a non-spherical particle as follows:

1. When the shortest particle–wall distance is the wall roughness amplitude (taken to be 10% of the particle diameter) one virtual wall is generated at the point of the particle which is closest to the wall. The virtual wall is generated with the original algorithm Konan et al. (2009), Sommerfeld and Huber (1999). This virtual wall is locally treated as deterministic, it remains at the location until all integration steps associated with the particle–wall collision are finished.
2. If the shortest particle–wall distance becomes half of the distance at which the virtual wall was inserted, *i.e.* the particle has moved closer to the wall, a second virtual wall is introduced, with a newly randomly sampled angle. This is shown in Fig. 4.
3. The addition of new virtual walls is repeated until the particle is moving away from the wall.

The required standard deviation for the normal distribution is taken from the experimental data provided by Kussin and Sommerfeld (2002). In the analysed flow, up to three virtual walls are required to deal with the rough wall collision, although almost all collisions are dealt with by application of a single rough wall.

Contact forces

The soft-sphere collision model is applied to resolve particle–particle and particle–wall collisions. The comparison between the hard-sphere and the soft-sphere model for spherical particles has been presented in Mallouppas and van Wachem (2013), showing that both are in good agreement for the channel flow conditions as studied in the current work. However, the hard-sphere model is not suitable for non-spherical particles and therefore a soft-sphere model has to be adopted.

The soft-sphere model essentially determines the slight overlap, or the displacement, of two particles or a particle and a wall. This

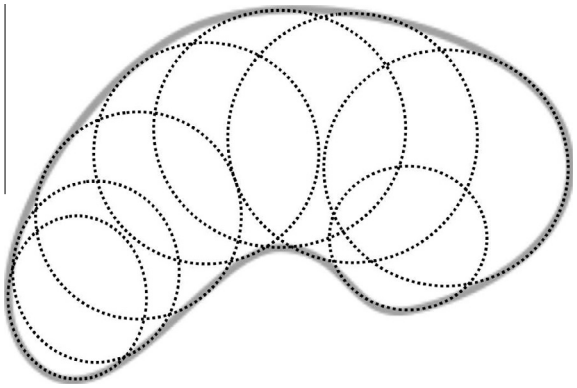

Fig. 3. An example of the body shown in Fig. 2 filled with 8 spheres. The spheres are used to find potential contact points with neighbouring particles or walls.

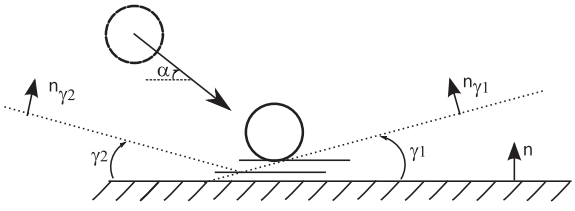

Fig. 4. An illustration of the newly proposed multiple virtual wall approach. A first virtual wall is introduced when the particle reaches the amplitude of the wall roughness added to the actual smooth wall. Additional virtual walls are added randomly every time the particle moves half of this amplitude closer to the wall. One such additional virtual wall is depicted.

overlap is used as a measure to estimate the local deformation of the particle at the point of collision, by assuming the contact point is locally axi-symmetric with a constant local radius, and leads to normal and tangential forces based upon Mindlin and Deresiewicz (1953),

$$\boldsymbol{F}_n(t) = K_n(t)\delta_n^{\frac{3}{2}}(t)\boldsymbol{n}(t)$$
$$\boldsymbol{F}_t(t) = \min\left(\mu\boldsymbol{F}_n(t), K_t(t)\boldsymbol{\delta}_t(t)\right)$$

where μ is the coefficient of friction, $\delta_n(t)$ is the scalar representing the normal displacement, $\boldsymbol{\delta}_t(t)$ is the vector representing the total tangential displacement mapped onto the current reference frame. The tangential displacement vector is determined by integrating the successive tangential displacements and mapping this into the current frame of reference of the collision. K_n and K_t are the spring constants for the normal and tangential forces respectively, as predicted Hertzian contact theory (Mindlin and Deresiewicz, 1953)

$$K_{n,l}(t) = \frac{4}{3}E^*\sqrt{r(t)}$$
$$K_t(t) = 8G^*\sqrt{r(t)\delta_t(t)}$$

where E^* represents the Young's modulus of the pair of colliding particles, G^* is the ratio of the Young's modulus and Poisson's ratio plus one for the pair of colliding particles, $r(t)$ represents the local radius of the particle (the distance from the centre of the particle to the contact point) and the subscript l represents loading, *i.e.* the particles moving towards each other. When the particles move away from each other, the subscript u, representing unloading will be used. To account for the dissipative nature of the collision, a coefficient of restitution is introduced to determine the spring constant value for unloading, represented by the subscript u, following Walton (1993)

$$e = \sqrt{\frac{K_{n,u}}{K_{n,l}}} \tag{32}$$

The total force on the body is determined by adding the gravity force, the fluid force, and summing the force contributions of all collisions of each particle

$$\boldsymbol{a}(t) = \boldsymbol{g} + \frac{\boldsymbol{F}_f(t)}{m_p} + \sum_{c=\text{contacts}} \frac{\boldsymbol{F}_{n,c}(t) + \boldsymbol{F}_{t,c}(t)}{m_p} \tag{33}$$

where m_p indicates the mass of the particle, $\boldsymbol{g}$ represents the gravitational acceleration, $\boldsymbol{F}_f$ represents the total interaction force with the fluid, and $\boldsymbol{F}_{n,c}$ and $\boldsymbol{F}_{t,c}$ represent the normal and tangential forces from the collision of the particle.

The torque on the body is determined by adding the torque arising from the fluid and the contributions of all collisions of each particle

$$\boldsymbol{\tau}(t) = \boldsymbol{\tau}_f(t) + \sum_{c=\text{contacts}} \left(\boldsymbol{p}_c - \boldsymbol{x}_p(t)\right) \times \left(\boldsymbol{F}_{n,c}(t) + \boldsymbol{F}_{t,c}(t)\right) \tag{34}$$

where $\boldsymbol{p}_c$ is the point of contact of the particle with another particle, and $\boldsymbol{x}_p$ is the centre of mass of the particle.

Fluid forces and torques on the particles

The fluid exerts two types of forces on the particle: drag force in the direction of the flow velocity and a transverse lift force. Additionally a pitching and counter-rotational torques are present. These interactions are given by the following equations (Zastawny et al., 2012):

$$F_D = C_D\frac{1}{2}\rho\tilde{v}^2\frac{\pi}{4}d_p^2 \tag{35}$$

$$F_L = C_L\frac{1}{2}\rho\tilde{v}^2\frac{\pi}{4}d_p^2 \tag{36}$$

$$\tau_P = C_T\frac{1}{2}\rho\tilde{v}^2\frac{\pi}{8}d_p^3 \tag{37}$$

$$\boldsymbol{\tau}_R = C_R\frac{1}{2}\rho\left(\frac{d_p}{2}\right)^5|\boldsymbol{\Omega}|\boldsymbol{\Omega} \tag{38}$$

where F_D are the drag force, F_L is the lift force, τ_P is the pitching torque, τ_R is the rotational torque, C_D, C_L, C_T and C_R are the shape specific force and torque coefficients, $\tilde{v} = \widehat{v}^f - v_p$ is the velocity of the particle relative to the local undisturbed fluid velocity, ρ is the fluid density, and d_p the equivalent particle diameter, *i.e.* the diameter of a sphere with the same volume as the considered particle. The relative rotation of the particle with respect to the fluid is given by

$$\boldsymbol{\Omega} = \frac{1}{2}\nabla\times\tilde{\boldsymbol{v}} - \boldsymbol{\omega}_p \tag{39}$$

with ω_p representing the angular velocity of the particle. The total fluid induced force is determined by adding the drag and lift forces and the total fluid induced torque is determined by adding the two torques.

As all of the considered particles in this paper are axi-symmetric, the force vector therefore consists of two principal components, the drag force acting in the direction of the flow, and the lift force acting in the perpendicular direction of the flow. Also because of the axi-symmetry of the particle, the effective angle between the flow and the longest axis through the body can be described by a single angle of incidence. The definition of this angle is shown in Table 1 for each of the particles. The angle of incidence is determined in body space, by transforming the local fluid velocity from world space to body space. The fluid velocity as seen by the particle in body space is computed as

$$\boldsymbol{v}^b(t) = q(t)\boldsymbol{v}(t)q^{-1}(t) \tag{40}$$

The angle of incidence is determined between the fluid velocity in body space and the x^b axis of the particle, corresponding to the unique principle axis of the particle, *i.e.* the length of the ellipsoid and the fibre and the thickness of the disc. Hence, the angle is determined as

$$\varphi = \left|\arctan\left(\frac{v_{sh}^b}{v_{ln}^b}\right)\right| \tag{41}$$

where v_{sh}^b is the velocity projection on the axis containing the smallest dimension of the body and v_{ln}^b is the projection of the velocity on the axis containing the longest dimension.

The consequent aerodynamic forces acting on the body *in body space* are then defined as

$$\boldsymbol{F}_D^b = \frac{1}{2}\rho\frac{1}{4}\pi d_{eq}^2 C_D(\varphi, Re)\left|\boldsymbol{v}^b\right|\boldsymbol{v}^b \tag{42}$$

$$F_L^b = \frac{1}{2}\rho\frac{1}{4}\pi d_{eq}^2 C_L(\varphi, Re)\left|\boldsymbol{v}^b\right|^2 \tag{43}$$

where the force coefficients depend on the angle of incidence and the local particle Reynolds number. Note that the lift force above is given as a scalar and is applied to the perpendicular direction of the fluid velocity. Therefore, the force components in the *body space* are the sum of drag and lift contributions and for the prolate ellipsoids have the following form,

$$F_{f,x}^b = \frac{1}{2}\cdot\rho\cdot\frac{1}{4}\pi d_{eq}^2\cdot C_D(\varphi, Re)\cdot|\boldsymbol{v}^b|v_x^b + F_L\cdot\sin\varphi\cdot sign(-v_x^b) \tag{44}$$

$$F_{f,y}^b = \frac{1}{2}\cdot\rho\cdot\frac{1}{4}\pi d_{eq}^2\cdot C_D(\varphi, Re)\cdot|\boldsymbol{v}^b|v_y^b + F_L\cdot\cos\varphi\cdot\frac{v_y^b}{\sqrt{v_y^{b^2}+v_z^{b^2}}} \tag{45}$$

$$F_{f,z}^b = \frac{1}{2}\cdot\rho\cdot\frac{1}{4}\pi d_{eq}^2\cdot C_D(\varphi, Re)\cdot|\boldsymbol{v}^b|v_z^b + F_L\cdot\cos\varphi\cdot\frac{v_z^b}{\sqrt{v_y^{b^2}+v_z^{b^2}}} \tag{46}$$

The specific expressions for the components are slightly different for the case of the disc, but follow the same idea. Once the forces are determined in the frame of body space, they are converted to world space and applied to the particle equation of motion.

Torques acting on the particles

When determining the torque on the particle, two mechanisms have to be considered. The first mechanism occurs if there is an oblique angle between the fluid velocity vector in body space and any of the principle axis of the body. When the position of the centre of pressure on the particle does not coincide with the centre of mass of the particle, a pitching torque will act in the axis perpendicular to the force plane. As the bodies considered in this paper are all axi-symmetric around the principal x^b axis, the contribution of this mechanism to the torque along the direction of the x^b axis in body space is always zero. The other two components for prolate ellipsoids are given by

$$\tau_y^b = \frac{1}{4}\rho\frac{1}{4}\pi d_{eq}^2 d_p C_T(\varphi, Re)\left|\boldsymbol{v}^b\right|\frac{\left|v_z^b\right|}{\sqrt{v_y^{b^2}+v_z^{b^2}}}\cdot sign(v_x^b v_z^b) \tag{47}$$

$$\tau_z^b = \frac{1}{4}\rho\frac{1}{4}\pi d_{eq}^2 d_p C_T(\varphi, Re)\left|\boldsymbol{v}^b\right|\frac{\left|v_y^b\right|}{\sqrt{v_y^{b^2}+v_z^{b^2}}}\cdot sign(v_x^b v_y^b) \tag{48}$$

Slightly modified expressions are applied in the case of particles with a disc-like shape, similarly as the correction to the lift force for this particle.

The second mechanism occurs if the body rotates with respect to the fluid framework of motion. In this case, the torque acts on the particle to counteract the rotation and is proportional to the angular velocity of the particle, as given by Eq. (38). In the case of axi-symmetric non-spherical particles it is reasonable to divide the rotation into two components, namely one along the primary axis of symmetry, *i.e.* along the axis x^b, and one axis perpendicular to this. Hence, the torque components in body space have the following form:

$$T_x^b = -C_R(\varphi, Re)\frac{\rho}{2}\left(\frac{d_p}{2}\right)^5 \Omega_x^{b^2} \tag{49}$$

$$T_y^b = -C_R(\varphi, Re)\frac{\rho}{2}\left(\frac{d_p}{2}\right)^5 |\boldsymbol{\Omega}_{yz}^b|\boldsymbol{\Omega}_y^b \tag{50}$$

$$T_z^b = -C_R(\varphi, Re)\frac{\rho}{2}\left(\frac{d_p}{2}\right)^5 |\boldsymbol{\Omega}_{yz}^b|\boldsymbol{\Omega}_z^b \tag{51}$$

where the angular velocity of the particle relative to the fluid in body space is denoted by $\boldsymbol{\Omega}$, and is determined by transforming Eq. (39) in body space.

It should be noted that the Saffman nor Magnus lift forces are not considered in the above analysis. This is the lift force caused by a local fluid velocity gradient over the particle. As the particles studied in this work have a high Stokes number, this contribution is assumed to be negligible.

Correlations for the drag, lift, pitching torque and rotational torque coefficients

The correlations for the drag, lift, pitching torque and rotational torque to predict the forces on the individual particles are taken from Zastawny et al. (2012). The equations have been validated for the same particle shapes as used in this research paper and have been determined as a function of angle of incidence (φ), the Reynolds number, and the rotational Reynolds number. The Reynolds number is defined with the equivalent particle diameter, d_p, as

$$Re = \frac{\rho^f u d_p}{\mu^f} \tag{52}$$

and the rotational Reynolds number is defined using the magnitude of the angular velocity

$$Re_R = \frac{\rho^f d_p^2 \omega}{\mu} \tag{53}$$

as the evaluation of the forces occurs in body space, the angular velocity of the particle in body space should be applied.

For the drag coefficient the expression which fits all the particle shapes best is given as (Zastawny et al., 2012)

$$C_D(\varphi) = C_{D,\varphi=0^o} + (C_{D,\varphi=90^o} - C_{D,\varphi=0^o})sin^{a_0}\varphi \tag{54}$$

where

$$C_{D,\varphi=0^o} = \frac{a_1}{Re^{a_2}} + \frac{a_3}{Re^{a_4}}$$

$$C_{D,\varphi=90^o} = \frac{a_5}{Re^{a_6}} + \frac{a_7}{Re^{a_8}}$$

where the a_i represent empirical parameters given in Table 2 for the various particle shapes.

The lift force considered is the force occurring if the flow is not aligned with one of the axes of symmetry of the particle. This lift is zero at 0 and 90 degrees. The expression for the lift force coefficient that describes this phenomenon is given as (Zastawny et al., 2012)

$$C_L = \left(\frac{b_1}{Re^{b_2}} + \frac{b_3}{Re^{b_4}}\right)sin(\varphi)^{b_5+b_6Re^{b_7}}cos(\varphi)^{b_8+b_9Re^{b_{10}}} \tag{55}$$

where b_i represent empirical parameters given in Table 2 for the various particle shapes.

Table 2
The values of fit parameters used in expressions for force coefficients of different particle shapes (Zastawny et al., 2012).

Coefficient	Ellipsoid 1	Ellipsoid 2	Disc	Fiber
a_0	2.0	1.95	1.96	2.12
a_1	5.1	18.12	5.82	20.35
a_2	0.48	1.023	0.44	0.98
a_3	15.52	4.26	15.56	2.77
a_4	1.05	0.384	1.068	0.396
a_5	24.68	21.52	35.41	29.14
a_6	0.98	0.99	0.96	0.97
a_7	3.19	2.86	3.63	3.66
a_8	0.21	0.26	0.05	0.16
b_1	6.079	0.083	12.111	8.652
b_2	0.898	−0.21	1.036	0.815
b_3	0.704	1.582	3.887	0.407
b_4	−0.028	0.851	0.109	−0.197
b_5	1.067	1.842	0.812	0.978
b_6	0.0025	−0.802	0.249	0.036
b_7	0.818	−0.006	−0.198	0.451
b_8	1.049	0.874	5.821	1.359
b_9	0.0	0.009	−4.717	−0.43
b_{10}	0.0	0.57	0.007	0.007
c_1	2.078	0.935	3.782	0.011
c_2	0.279	0.146	0.237	−0.656
c_3	0.372	−0.469	2.351	8.909
c_4	0.018	0.145	0.236	0.396
c_5	0.98	0.116	−0.394	2.926
c_6	0.0	0.748	1.615	−1.28
c_7	0.0	0.041	−0.044	0.037
c_8	1.0	0.221	−0.537	−15.236
c_9	0.0	0.657	1.805	16.757
c_{10}	0.0	0.044	−0.037	−0.006
r_1	0.23	0.573	3.812	0.024
r_2	−0.116	−0.154	−0.13	0.168
r_3	96.378	116.61	283.03	77.314
r_4	1.0	1.0	1.0	1.0

The pitching torque coefficient, C_T, is zero at the angles of incidence of 0 and 90 degrees. For the pitching torque coefficient, the expression is (Zastawny et al., 2012)

$$C_T = \left(\frac{c_1}{Re^{c_2}} + \frac{c_3}{Re^{c_4}}\right) sin(\varphi)^{c_5 + c_6 Re^{c_7}} cos(\varphi)^{c_8 + c_9 Re^{c_{10}}} \quad (56)$$

where c_i represent empirical parameters given in Table 2 for the various particle shapes.

The rotational torque is given by the expression (Zastawny et al., 2012):

$$C_R = r_1 (Re_R)^{r_2} + \frac{r_3}{(Re_R)^{r_4}} \quad (57)$$

where r_i represent empirical parameters given in Table 2 for the various particle shapes.

The form of these correlations is the same for all particle shapes, but the parameters in the correlations depend on the particle shape. These parameters are all displayed in Table 2.

The drag, lift and torque models as outlined above are the result of many true direct numerical simulations, which were presented in Zastawny et al. (2012). In these true direct numerical simulations all the flow structures are resolved, and the interaction of the particles with the fluid is determined without any assumption. The models have been validated by grid refinement, and match the analytical expression for the drag, lift and torque proposed by Brenner (1964) and Jeffery (1922) for cases in which the Reynolds number approaches zero. Moreover, the flow patterns and findings of these models are in agreement with the experimental findings of Hoerner (1965) and the computational work of Hölzer and Sommerfeld (2008).

Simulation details

Set-up

The large-scale simulations are performed in the Eulerian–Lagrangian framework and the predictions are compared to the experimental work of Kussin and Sommerfeld (2002). In their work, a horizontal channel with a height of 35 mm, a width of 175 mm and a length of 6 m, corresponding to approximately 170 channel heights. A flow of an air-particle mixture with various particle sizes and mass loadings is introduced in the horizontal direction. The mass loading is defined as the ratio of the mass particles introduced in the domain with the mass of the fluid (*i.e.* air) in the same domain.

This paper focuses on the experimental results obtained by Kussin and Sommerfeld (2002), for the two-phase flow with mass loading, $\phi = 1.0$, with the particles of 195 μm. At this mass loading both fluid-particle as well as particle–particle interactions are expected to be important. The experimental Reynolds number considered based on the channel height is 42,585, arising from the average air velocity of $U_{av} = 19.7$ m/s, air density of $\rho_f = 1.15$ kg/m^3 and a viscosity of $\mu_f = 18.62$ Pa s. The friction Reynolds number based on the half channel height is $Re_\tau = 600$. The particles considered are glass beads, $\rho_p = 2500$ kg/m^3. In the simulations, particles are tracked for 47 T_L, where T_L is the Lagrangian integral time scale of turbulence at the centre of the channel. The Stokes number of the particles depends on the changing fluid timescale. The Stokes number is much larger than one, irrespective of location or precise definition. The simulations are carried out in a three-dimensional domain of 0.175 m × 0.035 m × 0.035 m, where the X direction corresponds to the direction of the flow and the Y direction is the direction of gravity. The X and Z directions are taken to be periodic and the lengths of the domain in these directions has been verified to not affect the results. The domain used for the simulations is sketched in Fig. 5.

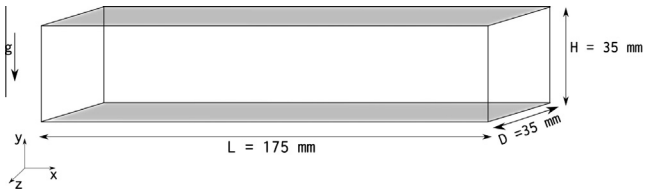

Fig. 5. The geometry of the channel as used in the simulations. The mean flow is in the X direction and the gravity is in the Y direction. Both the X and Z directions are periodic for the flow and the particles. The walls of the channel are indicated in grey.

The simulations are carried out with the in-house code Multiflow (van Wachem et al., 2012; Mallouppas and van Wachem, 2013; Denner and van Wachem, 2014), which is a fully coupled parallel computational fluid dynamics code based on finite volume discretisation and various types of particle and fluid models.

Initial and boundary conditions

The the flow is initialised by setting a mean velocity of 19.7 m/s based on the Reynolds number. On top of the mean, synthesised turbulence is added as randomly sampled from a von Karman spectrum, using the Fourier modes of the fully developed turbulent spectrum. The initial condition does not impose a flow profile; the flow profile is formed as a result of solving the Navier–Stokes equations and enforcing the no-slip condition for velocity at the wall. The boundary conditions at the walls are set as no-slip conditions. A constant forcing term is introduced everywhere in the flow domain to keep a constant mass flow rate, $\dot{m} = 0.027044$ kg/s, matching the pressure drop required to overcome the wall shear stress in equilibrium. The average resulting pressure drop equals the total wall shear stress in the channel. The pressure is fixed to a reference value on one arbitrary cell face inside the domain. The pressure on the wall faces is determined by extrapolation from the flow domain.

The particles are introduced uniformly in the domain with a small random slip velocity compared to the local fluid velocity. The number of particles in the domain is determined by the mass loading and is 24,000 corresponding to a mass loading of $\phi = 1$.

Computational mesh

The computational mesh contains a total of 870,000 computational cells and the wall boundary layer is resolved by 5 mesh poins within the $y^+ = 10$ layer. Near the wall a DNS resolution is obtained by using the y-coordinate for the nth gridpoint:

$$y_n = y_{max}\left[\frac{1}{2}\left[\frac{1 + \tanh\left(R\frac{n\Delta y}{y_{max}} - \frac{1}{2}\right)}{\tanh(\frac{1}{2}R)}\right]\right] \quad (58)$$

where R is a constant set to 7.0 and defines the amount of refinement near the wall, Δy is the average mesh spacing, and $y_{max} = 35.0$ mm, is the channel height. In addition, in every $x^+ = 50$ and $z^+ = 30,1$ mesh point is uniformly added.

Mesh refinement results have been presented in Mallouppas and van Wachem (2013), showing that the applied mesh is sufficiently fine to capture the flow details. Moreover, spectra of the single-phase flow computations are presented in Mallouppas and van Wachem (2013), showing that all the energetic eddies are captured satisfactorily by the mesh and the assumptions for LES are met. The results of these simulation are in very good agreement with the experimental results of Kussin and Sommerfeld (2002).

Discretisation

The discretisation of the Navier–Stokes equations is done using a finite volume approach, combined with a second order accurate three point backward Euler time discretisation for the temporal terms and a second order accurate central differencing scheme for the advection term. The pressure velocity coupling is done in a fully coupled framework, using one outer iteration per time-step. This outer iteration is solved with typically 4 iterations of the stabilised bi-conjugate gradient stabilised method using incomplete LU decomposition to precondition the linearised matrix.

Fluid-particle coupling

As the particles move in a Lagrangian framework and the fluid is solved in a fixed Eulerian framework, the coupling between these frameworks requires special attention. The fluid velocity as determined on the Eulerian mesh must be accurately interpolated to each of the Lagrangian particles. Some properties of interpolation schemes between the Eulerian and the Lagrangian frameworks are discussed in Franklin and Lee (2010). A frequently used interpolation scheme is the tri-linear interpolation, which has a number of favourable properties, such as continuity and ease of implementation, but suffers from a strong filtering of higher frequency velocity fluctuations and is probably not suitable for LES. Therefore, we have used a polynomial spline interpolation, where a property of the fluid at the particle is approximated by

$$\phi_{f@p} = \sum_{n=1}^{N} \sum_{i,j,k}^{I,J,K} a_{n,ijk} \Delta x^i \Delta y^j \Delta z^k \phi_{f,n} \tag{59}$$

where the summation over n is over the independent points and the summation over (i,j,k) is over the polynomial integer values, and $a_{n,ijk}$ is the constant coefficient corresponding to independent point n and the polynomial powers of (i,j,k) for the three directions. The number of independent fluid velocity points, N, used to evaluate the spline is 27, and the order of the polynomial used is, therefore $(I,J,K) = (3,3,3)$.

Results and discussion

The simulations were performed on the HPC facility of Imperial College London, using 16 cores per simulation. Simulations of the single-phase flow and simulations of spherical particles have been presented in Mallouppas and van Wachem (2013). This article will focus on the flow with non-spherical particles. The simulations with the non-spherical particles take approximately 40 h of computational time on 16 cores to achieve steady-state statistics for the particle phase. It is observed that it takes much longer time for the statistics of the particle phase to become steady than for the fluid phase. Simulations with non-spherical particles are approximately 30% more computationally expensive than the simulations of spheres. This is due to the fact that the orientation of the particle has to be resolved, requiring a significantly smaller time-step compared to the spheres. are steady. From the initial conditions, simulations have run for 35 T_L before starting to sample data, and the sampling is done for a time duration of 7 T_L. T_L represents the Lagrangian integral time scale of turbulence at the centre of the channel. It has been verified that the obtained statistics are steady.

The plane averaged relative concentration for all shapes of particles considered in this study as a function of height in the channel is shown in Fig. 6 for the experiments (spheres) and all the simulations, for both the cases considering the effect of wall roughness and neglecting wall roughness, indicated as smooth walls in the figure. The relative concentration is calculated by averaging the number of particles in each horizontal plane, and normalising this average throughout the channel. Simulations without considering the effect of wall roughness show that the particles tend to graze near the bottom of the channel, as the relative concentration is much higher near the bottom than near the top. The reason for this is that next to turbulent dispersion and particle–particle collisions, which are both very weak phenomena in this case, there is no mechanism to re-suspend the particles back into the bulk of the flow. This effect is even more pronounced with non-spherical particles as their orientation changes significantly, compared to in the bulk of the flow, as they graze near the bottom of the channel. Because non-spherical particles in the near wall region align along the wall, the concentration becomes even higher compared to spherical particles. This effect is strongest for fibres and discs, as can be expected from these strongly elongated shapes.

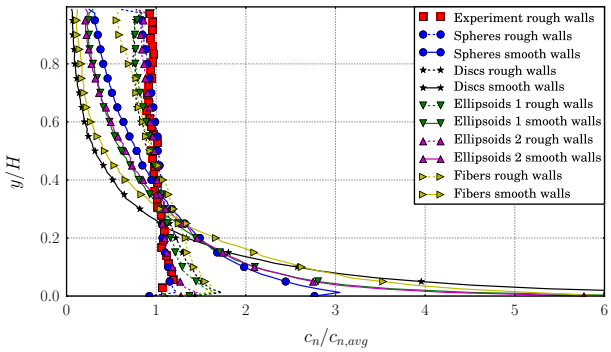

Fig. 6. The relative particle concentration for all considered particles, as a function of dimensionless channel height for the simulation without considering wall roughness, the simulation considering wall roughness, and the experimental measurements for spherical particles from Kussin and Sommerfeld (2002).

Including the effect of rough walls in the simulation changes the concentration profiles enormously. Fig. 7 shows an instantaneous distribution of the location of the fibres for the simulation considering the effect of wall roughness, (a), and the simulation neglecting this effect, (b). It can be clearly seen that in case (a) the fibres are fairly homogeneously distributed in the channel, whereas for case (b) the fibres tend to flow in the bottom part of the channel. The wall roughness provides an additional mechanism for transferring momentum from the horizontal direction into the vertical direction. Even though this effect is not very strong, it is sufficient to enable the spherical particles to move through the channel so that there is almost no concentration gradient in the vertical direction, as observed by the experiment Kussin and Sommerfeld (2002) as well as earlier simulations of spheres, reported in Mallouppas and van Wachem (2013).

There are significant changes when considering the behaviour of non-spherical particles compared to spherical ones. Fig. 8 shows the relative concentration profiles for all the shapes of particles and the experimental data from Kussin and Sommerfeld (2002) for rough walls only. For spherical particles, the effect of the wall roughness is sufficient to re-suspend the spheres into the flow. The collisions with the rough wall provide an additional, stronger, mechanism for converting momentum from the horizontal direction into the vertical direction. However, for non-spherical particles a significant part of the horizontal momentum is not converted to vertical translational momentum by a collision with a rough wall, but to rotational momentum. The non-spherical particles tend to rotate more strongly in the near-wall region due to the rough walls, and this rotational momentum does not contribute to re-suspending particles back into the flow. Therefore, the effect of rough walls is not as pronounced for non-spherical particles as it is for the spheres, as can be clearly seen from Fig. 8.

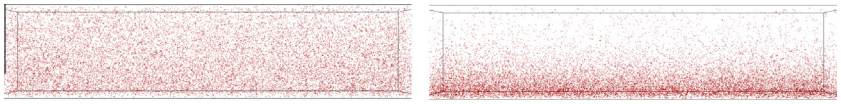

Fig. 7. Instantaneous distribution of the fibres for simulations when the statistics have reached steady state for: (a) considering the effect of wall roughness, and (b) neglecting the effect of wall roughness.

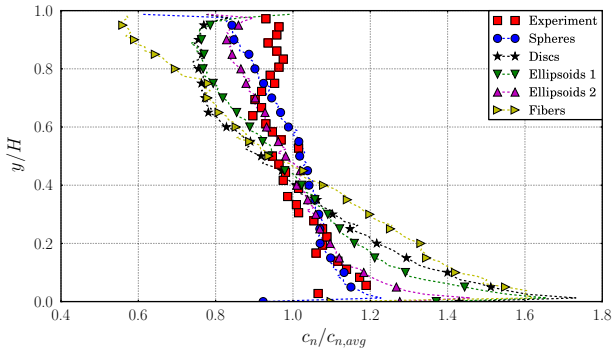

Fig. 8. The relative particle concentration for all considered particles, as a function of dimensionless channel height for the simulations considering wall roughness, and the experimental measurements for spherical particles from Kussin and Sommerfeld (2002).

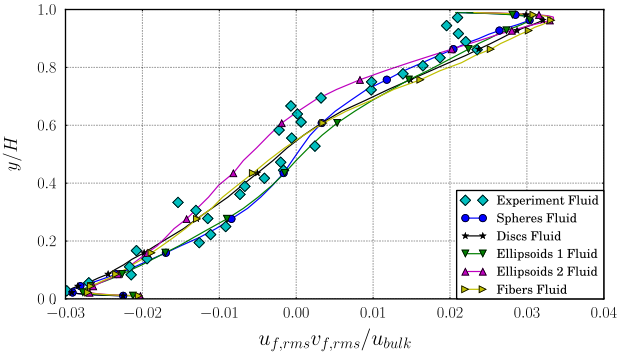

Fig. 10. The Reynolds stresses of the fluid for the all the considered particle shapes, as a function of dimensionless channel height and the experimental measurements for the fluid containing spherical particles from Kussin and Sommerfeld (2002).

The particle and corresponding fluid velocities for all shapes of particles including and excluding the effect of wall roughness are shown in Fig. 9. The velocity of the spheres and the experimental measurements are in very good agreement with each other. Also, the velocity of the fluid is in good agreement with the experimental measurements. It is observed that all the non-spherical particles flow faster through the channel than the spherical particles. This is because the non-spherical particles tend to locally maximise the drag force, by aligning their longest axis perpendicular to the local flow direction. The fluid profiles are slightly influenced by the particles, as can be seen from the variations in fluid velocity shown in Fig. 9. However, there is very little effect of the particles on the fluid Reynolds stresses if the flow, as can be seen from Fig. 10.

The plane averaged particle velocities predicted by the simulations including wall roughness are compared to the particle velocities resulting from simulations excluding wall roughness in Fig. 11. For the simulations including the effect of wall roughness, the particle velocity profiles are more or less symmetrical, but the simulations without wall roughness show a strong asymmetric profile, due to the very strong concentration gradient as earlier shown in Fig. 6, especially for the non-spherical particles.

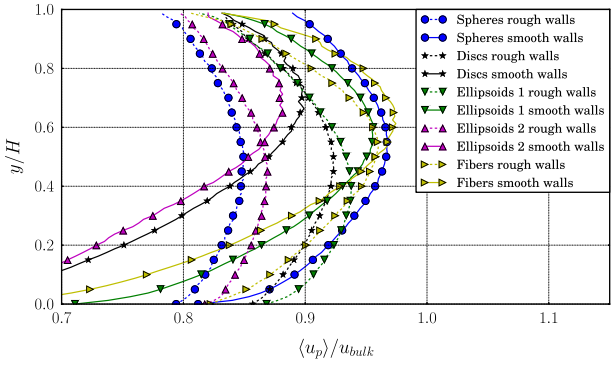

Fig. 11. The average particle velocities for all considered particles as a function of dimensionless channel height for the simulations considering the effect of wall roughness compared to the simulations excluding the effect of wall roughness.

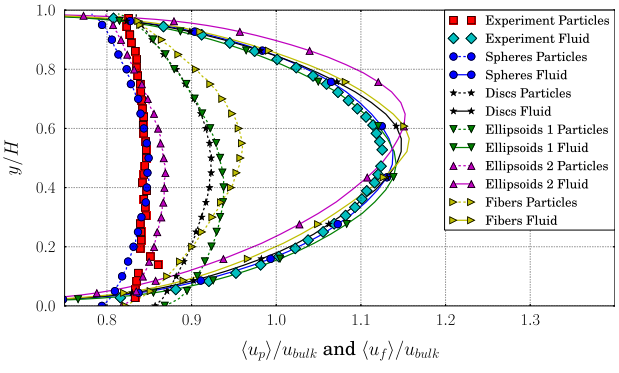

Fig. 9. The average particle and fluid velocities for all considered particles, as a function of dimensionless channel height for the simulations considering the effect of wall roughness and the experimental measurements for spherical particles from Kussin and Sommerfeld (2002).

It can be concluded from Figs. 6, 8, 9, and 11 that ellipsoids 2 almost behave as the spherical particles, which again match very well with the experimental measurements. The particle concentration as a function of channel height, as well as the particle velocity as a function of channel height are very close to those of the spheres. This can be seen as a *validation* of the computational framework, as the sphericity of ellipsoids 2 is near unity, 0.99.

The average angle of attack of the non-spherical particles is shown in Fig. 12. As confirmed by the average velocities of the particles, shown in Fig. 9, the particles tend to align their longest axis perpendicular to the flow, hereby maximising their local drag. This results in a high average angle of attack, a high particle flow velocity, and a higher pressure drop, compared to the spheres. Near the walls, the effect of the collisions can be clearly seen. A measure for the oscillation or rotation of the particles is the root mean square of the fluctuations of the angle of attack, shown in Fig. 13 as a function of channel height. The disc-shaped particle has the highest average angle of attack, over 70°, and the lowest root mean square

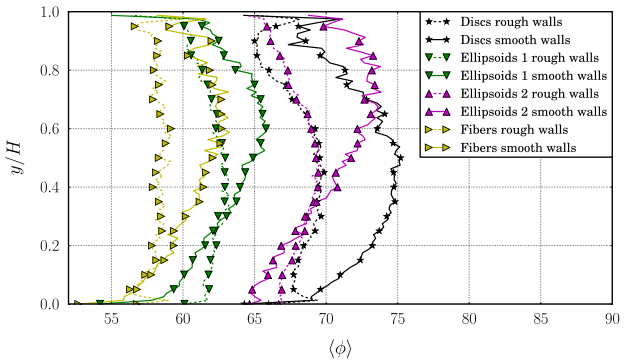

Fig. 12. The average angle of attack for the non-spherical particles, as a function of dimensionless channel height for the simulations without considering wall roughness and the simulations considering wall roughness.

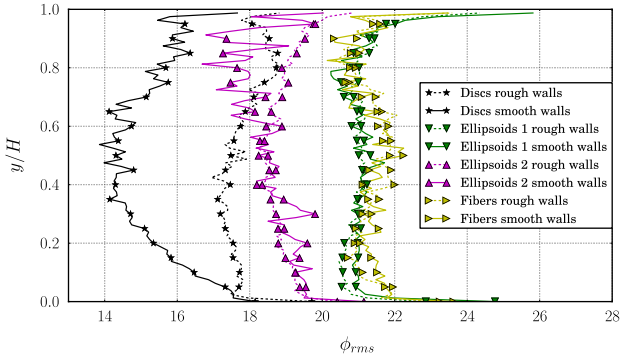

Fig. 13. The root mean square of the fluctuating angle of attack for the non-spherical particles, as a function of dimensionless channel height for the simulations without considering wall roughness and the simulations considering wall roughness.

fluctuating angle of attack, so this shape oscillates the least, closely followed by ellipse number 2. Of all the shapes considered in this paper, the disc-shaped particle shows the most stable flow. The fibre shaped particle and ellipse number 1 show the lowest average angle of attack, although it is still well above 55°. However, the root mean square of the fluctuating angles is quite large for both the fibre as well as ellipse number 1. This is because the fibre shape and the elongated ellipse shape exhibit the least stable flow behaviour compared to the other non-spherical shapes, making these shapes relatively sensitive to fluid velocity fluctuations.

The wall roughness seems to have a small effect on the average angle of the particles, as it de-stabilises the position of the particle a little. When a non-spherical particle collides with a wall, rotation of the particle is induced. A particle collision with a rough wall induces slightly more rotation, leading to a smaller average angle of attack. This can be observed from the difference in average angle of attack between simulations incorporating rough walls compared to where this effect is neglected in Fig. 12. This is also consistent with the observation that the root mean square of the fluctuating angle of attack is higher in cases incorporating wall roughness as shown in Fig. 13.

Conclusions

This paper describes a complete framework to predict the behaviour of interacting non-spherical particles with large Stokes numbers in a turbulent flow. A summary of the rigid body dynamics of particles is presented in the framework of Quaternions, showing a novel algorithm to convert tensors from body space to world space as well as a novel algorithm to integrate unit Quaternions efficiently. This new approach does not rely on the renormalisation of the Quaternion, but uses a method which inherently conserves the unity of the Quaternion in time. The integration framework for Quaternions has been scrutinised and validated by Zhao and van Wachem (2013b).

To describe the interaction of the non-spherical particles with the fluid, the drag and lift forces and the torque are determined through the closures determined from DNS as described and validated in Zastawny et al. (2012). The collisions between the particles themselves and the particles and the walls are also taken into account. This is achieved by identifying all the contact points of the particles, and determining a collision force assuming a visco-elastic deformation in the contact point. A subsequent repulsive force is determined acting at the point of contact, leading to a force and a torque on the particle. Finally, a model to deal with the interaction of rough walls and particles using a visco-elastic approach is applied to non-spherical particles.

The framework is applied to turbulent channel flow, of which the experiments for spherical particles are presented in Kussin and Sommerfeld (2002). Five differently shaped particles are considered in this flow, each with an equivalent diameter of around $d_p = 195$ μm and a mass loading of $\phi = 1$, matching the experimental parameters of Kussin and Sommerfeld (2002). The channel flow is resolved with a hybrid DNS-LES approach. The results for single-phase flow and the flow laden with spherical particles is in very good agreement, and has been reported in Mallouppas and van Wachem (2013). Moreover, the results of nearly spherical ellipsoids, with a sphericity factor of 0.99, are very close to those of the spheres, which serves as an additional validation of the complete framework.

From the results of the flow of non-spherical particles, it is generally observed that non-spherical particles try to locally maximise their drag, although the inertia of the particles and the local fluid velocity fluctuations and gradients prevent this from occurring instantaneously. This phenomena is further investigated in this paper by performing resolved true direct numerical simulations of a non-spherical particle in a flow. These results show that in case of slip between the particle and the fluid, two pressure gradients on the acute sides of the particle exist, and cause a net torque if the axis of the particle is not exactly perpendicular to the flow direction. The only stable orientation of the particle is if the longest axis of the particle is aligned perpendicular to the flow direction. This phenomenon is not captured by using the torque model of Jeffery (1922), which is used by other research papers, because it is derived for flow situations where there is no slip velocity between the particles and the fluid.

The average angle between the longest axis of the non-spherical particles and the direction of the average flow channel is as high as 70°. Because of this effect, the non-spherical particles move considerably faster through the channel than the spherical particles. This also results in a larger pressure drop. The disc-shaped particle exhibits the most stable flow behaviour, with the highest average angle and the lowest root mean square of fluctuation of angle. This can be explained by the fact that the acute angle of the disc is the sharpest compared to the other particle shapes. On the other hand, the elongated fibre shows the least stable behaviour; it shows the most oscillating motion around its axes as it moves through the channel.

The wall roughness has a very important effect on the flow of non-spherical particles, even more so than for spherical particles. Non-spherical particles that are grazing near the bottom of the channel are returned into the flow by the roughness, but the roughness also induces additional rotation of the non-spherical particles. This leads to a lower mean angle between the shortest axis of the particle and the average channel flow direction and a higher fluctuating angle.

Acknowledgements

The authors are grateful to the Engineering and Physical Sciences Research Council (EPSRC) for their financial support (Grant No. EP/G049262/1).

The authors would like to thank Prof. M. Sommerfeld for providing the experimental data. The authors are also grateful to the European Cooperation in Science and Technology (COST) Action FP 1005 on "*fiber suspension flow modelling*" for the fruitful meetings and discussions.

References

Allen, M.P., Tildesley, D.J., 1989. The Computer Simulation of Liquids, vol. 42. Oxford University Press.
Betsch, P., Siebert, R., 2009. Rigid body dynamics in terms of quaternions: Hamiltonian formulation and conserving numerical integration. Int. J. Numer. Methods Eng. 79, 444–473.
Brenner, H., 1964. The Stokes resistance of an arbitrary particle-IV Arbitrary fields of flow. Chem. Eng. Sci. 19, 703–727.
Chhabra, R., Agarwal, L., Sinha, N., 1999. Drag on non-spherical particles: an evaluation of available methods. Powder Technol. 101, 288–295.
Crowe, C.T., 2005. Multiphase Flow Handbook. CRC Press.
Delaney, G.W., Cleary, P., 2010. The packing properties of superellipsoids. EPL (Europhys. Lett.) 89, 34002.
Denner, F., van Wachem, B., 2014. Fully-coupled balanced-force VOF framework for arbitrary meshes with least-squares curvature evaluation from volume fractions. Numer. Heat Transfer, Part B: Fundam. 65, 218–255.
Eberly, D., 2002. Quaternion Algebra and Calculus, vol. 21. Magic Software, Inc, pp. 1–10.
Evans, D., Murad, S., 1977. Singularity free algorithm for molecular dynamics simulation of rigid polyatomics. Mol. Phys. 34, 327–331.
Fan, L.S., Zhu, C., 1998. Principles of Gas-Solid Flows. Cambridge Univ. Press.
Franklin, J.D., Lee, J.S., 2010. A high quality interpolation method for colocated polyhedral/polygonal control volume methods. Comput. Fluids 39, 1012–1021.
Fukagata, K., Zahrai, S., Bark, F.H., 2001. Effects of wall roughness in a gas-particle turbulent vertical channel flow. In: Proc. 2nd Int. Symp. on Turbulence and Shear Flow Phenomena, KTH, Stockholm. vol. II, pp. 117–122.
Germano, M., Piomelli, U., Moin, P., Cabot, W.H., 1991. A dynamic subgrid-scale eddy viscosity model. Phys. Fluids A 3, 1760–1765.
Gsponer, A., Hurni, J.-P., 1993. The physical heritage of Sir W.R. Hamilton. In: The Mathematical Heritage of Sir William Rowan Hamilton - commemorating the sesquicentennial of the invention of quaternions. Trinity College, Dublin, pp. 1–37.
Hamilton, W.R., 1844. On quaternions; or on a new system of imaginaries in Algebra. London Edinburgh Dublin Philos. Mag. J. Sci. (3rd Ser.), 1–306.
Hoerner, S.F., 1965. Fluid-Dynamic Drag: Practical Information on Aerodynamic Drag and Hydrodynamic Resistance. Hoerner, Brick Town.
Hoffmann, G., 1978. Application of Quaternions. Tech. Rep. February 1978, Technische Universität Braunschweig.
Hölzer, A., Sommerfeld, M., 2008. New simple correlation formula for the drag coefficient of non-spherical particles. Powder Technol. 184, 361–365.
Ibanez, L., 2001. Tutorial on Quaternions Part I. Tech. Rep. 8, Insight Segmentation and Registration Toolkit, ITK.
Jeffery, G.B., 1922. The motion of ellipsoidal particles immersed in a viscous fluid. Proc. R. Soc. London. Ser. A, Containing Papers Math. Phys. Character 102, 161–179.
Karney, C.F.F., 2007. Quaternions in molecular modeling. J. Mol. Graphics Modell. 25, 595–604.
Konan, N.A., Kannengieser, O., Simonin, O., 2009. Stochastic modeling of the multiple rebound effects for particle – rough wall collisions. Int. J. Multiph. Flow 35, 933–945.
Konan, N.A., Simonin, O., Squires, K.D., 2011. Detached eddy simulations and particle Lagrangian tracking of horizontal rough wall turbulent channel flow. J. Turbul. 12, 1–21.
Kuang, S.B., Chu, K.W., Yu, A.B., Zou, Z.S., Feng, Y.Q., 2008. Computational investigation of horizontal slug flow in pneumatic conveying. Ind. Eng. Chem. Res. 47, 470–480.
Kulick, J., Fessler, J., Eaton, J., 1994. Particle response and turbulence modification in fully developed channel flow. J. Fluid Mech. 277, 109–134.
Kussin, J., Sommerfeld, M., 2002. Experimental studies on particle behaviour and turbulence modification in horizontal channel flow with different wall roughness. Exp. Fluids 33, 143–159.
Lain, S., Sommerfeld, M., 2007. A study of the pneumatic conveying of non-spherical particles in a turbulent horizontal channel flow. Braz. J. Chem. Eng. 24, 535–546.
Langston, P.A., Al-Awamleh, M.A., Fraige, F.Y., Asmar, B.N., 2004. Distinct element modelling of non-spherical frictionless particle flow. Chem. Eng. Sci. 59, 425–435.
Lilly, D.K., 1992. A proposed modification of the Germano subgrid scale closure method. Phys. Fluids A 4, 633–635.
Mallouppas, G., van Wachem, B., 2013. Large Eddy Simulations of turbulent particle-laden channel flow. Int. J. Multiph. Flow 54, 65–75.
Mandø, M., Rosendahl, L., 2010. On the motion of non-spherical particles at high Reynolds number. Powder Technol. 202, 1–13.
Marchioli, C., Soldati, A., 2013. Rotation statistics of fibers in wall shear turbulence. Acta Mech. 224, 2311–2329.
Marchioli, C., Fantoni, M., Soldati, A., 2010. Orientation, distribution, and deposition of elongated, inertial fibers in turbulent channel flow. Phys. Fluids 22, 033301.
Mark, A., van Wachem, B., 2008. Derivation and validation of a novel implicit second-order accurate immersed boundary method. J. Comput. Phys. 227, 6660–6680.
Mindlin, R.D., Deresiewicz, H., 1953. Elastic spheres in contact under varying oblique forces. J. Appl. Mech. 20, 327–344.
Minier, J.P., Peirano, E., 2001. The pdf approach to turbulent polydispersed two-phase flows. Phys. Rep. 352, 1–214.
Mittal, R., Iaccarino, G., 2005. Immersed boundary methods. Annu. Rev. Fluid Mech. 37, 239–261.
Njobuenwu, D.O., Fairweather, M., 2013. Effect of shape on inertial particle dynamics in a channel flow. Flow Turbul. Combust. 92, 83–101.
Patankar, N., Singh, P., Joseph, D., Glowinski, R., Pan, T., 2000. A new formulation of the distributed Lagrange multiplier/fictitious domain method for particulate flows. Int. J. Multiph. Flow 26, 1509–1524.
Portela, L., Oliemans, R., 2003. Eulerian – Lagrangian DNS/LES of particle – turbulence interactions in wall-bounded flows. Int. J. Numer. Methods Fluids 43, 1045–1065.
Sagaut, P., 2005. Large Eddy Simulation for Incompressible Flows, 3rd ed. Springer.
Simonin, O., Deutsch, E., Minier, J.P., 1993. Eulerian prediction of the fluid/particle correlated motion in turbulent two-phase flows. Appl. Sci. Res. 51, 275–283.
Snyder, W.H., Lumley, J.L., 1971. Some measurements of particle velocity autocorrelation functions in a turbulent flow. J. Fluid Mech. 48, 41–71.
Sommerfeld, M., 1992. Modelling of particle-wall collisions in confined gas-particle flows. Int. J. Multiph. Flow 18, 905–926.
Sommerfeld, M., 2003. Analysis of collision effects for turbulent gas-particle flow in a horizontal channel: Part I. Particle transport. Int. J. Multiphase Flow 29, 675–699.
Sommerfeld, M., Huber, N., 1999. Experimental analysis and modelling of particle-wall collisions. Int. J. Multiph. Flow 25, 1457–1489.
Sommerfeld, M., Kussin, J., 2003. Analysis of collision effects for turbulent gas-particle flow in a horizontal channel. Part II. Integral properties and validation. Int. J. Multiphase Flow 29, 701–718.
Sommerfeld, M., Kussin, J., 2004. Wall roughness effects on pneumatic conveying of spherical particles in a narrow horizontal channel. Powder Technol. 142, 180–192.
Tsuji, Y., 1993. Discrete particle simulation of gas-solid flows. KONA, 11.
Tsuji, Y., Morikawa, Y., Tanaka, T., 1987. Numerical simulation of gas–solid two-phase flow in a two-dimensional horizontal channel. Int. J. Multiph. Flow 13, 671–684.
Tsuji, Y., Tanaka, T., Ishida, T., 1992. Lagrangian numerical simulation of plug flow of cohesionless particles in a horizontal pipe. Powder Technol. 71, 239–250.
van Wachem, B., Schouten, J., van den Bleek, C., Krishna, R., Sinclair, J., 2001a. Comparative analysis of CFD models of dense gas solid systems. AIChE J. 47.
van Wachem, B., Van der Schaaf, J., Schouten, J., Krishna, R., van den Bleek, C., 2001b. Experimental validation of Lagrangian–Eulerian simulations of fluidized beds. Powder Technol. 116, 155–165.
van Wachem, B., Zastawny, M., Mallouppas, G., Zhao, F., Denner, F., Pennefather, J.C., 2012. <http://www.multiflow.org/>.
Vreman, A.W., 2007. Turbulence characteristics of particle-laden pipe flow. J. Fluid Mech. 584, 235.
Wadell, H., 1934. The coefficient of resistance as a function of Reynolds number for solids of various shapes. J. Franklin Inst. April, 459–490.
Walton, O.R., 1993. Numerical simulation of inclined chute flows of monodisperse, inelastic, frictional spheres. Mech. Mater. 16, 239–247.
Zastawny, M., Mallouppas, G., Zhao, F., van Wachem, B., 2012. Derivation of drag and lift force and torque coefficients for non-spherical particles in flows. Int. J. Multiph. Flow 39, 227–239.
Zhao, F., van Wachem, B., 2013a. Direct numerical simulation of ellipsoidal particles in turbulent channel flow. Acta Mech. 224, 2331–2358.
Zhao, F., van Wachem, B.G.M., 2013b. A novel Quaternion integration approach for describing the behaviour of non-spherical particles. Acta Mech. 224, 3091–3109.